

Extracting the Solution of Three-Dimensional Wave Diffraction Problem from Two-Dimensional Analysis by Introducing an Artificial Neural Network for Floating Objects

Meisam Qorbani Fouladi^a , Peyman Badiei^{a*} , Shahram Vahdani^a 

^a School of civil engineering, college of engineering, University of Tehran, Tehran, Iran. E-mails: meisam.qorbani@ut.ac.ir, pbadie@ut.ac.ir, svahdani@ut.ac.ir

*Corresponding author

<https://doi.org/10.1590/1679-78256096>

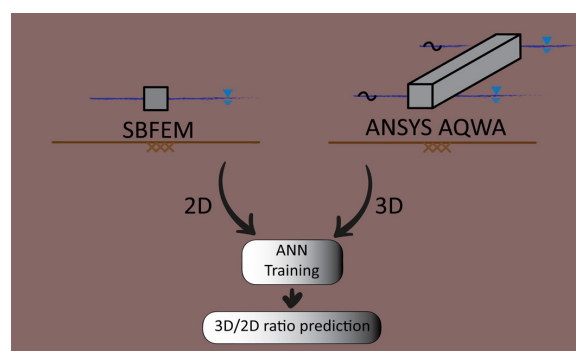
Abstract

The diffraction of the waves from the two ends of floating breakwaters (FBWs) that have limited length, are practically a three-dimensional (3D). In order to perform a two-dimensional vertical (2DV) analysis to solve the wave diffraction problem, some “correcting factors” are required to modify the 2DV results and make them comparable and verifiable against 3D solutions. The main objective of the current study is to propose a method to obtain these correcting factors and demonstrate its usefulness through some example cases. An Artificial Neural Network (ANN) is trained by three main non-dimensional independent variables to predict the mentioned factors. In order to set up the ANN, a database including both 2DV and 3D results is required. The 2DV results are obtained by employing a semi-analytical method, namely the Scaled Boundary Finite Element Method (SBFEM). A basic change in the location of the scaling center is implemented. The 3D results are obtained via ANSYS AQWA software. Eighty-one cases are simulated on a floating object with rectangular cross-sections. The correlation factor $R = 0.9607$ for a group of new samples shows that the predicted results are closely matched to the target values. The correcting factor applies the 3D effects of diffracted waves around the structures on 2DV results and produces a more accurate prediction.

Keywords

Scaled Boundary Finite Element Method, Water Wave Diffraction, Artificial Neural Network

Graphical Abstract



Received: May 04, 2020. In Revised Form: September 14, 2020. Accepted: September 21, 2020. Available online: October 08, 2020.

<https://doi.org/10.1590/1679-78256096>



Latin American Journal of Solids and Structures. ISSN 1679-7825. Copyright © 2020. This is an Open Access article distributed under the terms of the Creative Commons Attribution License, which permits unrestricted use, distribution, and reproduction in any medium, provided the original work is properly cited.

1 INTRODUCTION

The relationship between man-made structures and the ocean environment is an essential issue in Oceanic Engineering. Since all the structures in offshore and coastal areas - such as Floating Breakwaters (FBWs) - are exposed to water waves, it is necessary to analyze the effects of such structures on the surrounding wave domain (Abbasnia and Ghiasi (2014); Shahrabi and Bargi (2019)). By assuming linear waves and employing the superposition principle, in the investigation of wave-floating structures interaction, two distinct phenomena should be considered (Abul-Azm and Gesraha, 2000; Kao et al., 2015; Cho, 2016). The first phenomenon consists of a forced vibration assumption for structure and calculating radiated waves in non-disturbed fluid media. The second is to do with scattered waves by a stationary structure in a fluid domain exposed to incident waves. In the present work, the concentration is on wave scattering phenomenon. The configuration of the model and numerical procedures for calculating the scattered waves by FBWs and excitation wave forces would result in common challenges in the investigation processes. Numerous works have been devoted to the wave diffraction problem by FBWs.

From the configuration point of view, the majority of floating breakwaters have a long length, which is the reason why the majority of the previous researches offered studies based on the two-dimensional vertical (2DV) analysis. For example, by considering three degrees of freedom for the motion of structure, Abul-Azm and Gesraha (2000) examined the wave-structure interaction problems and the factors affecting the pontoon performance. Zheng et al. (2004a, 2004b) studied the diffraction and radiation problems in an infinite and semi-infinite fluid domain with constant water depth, respectively. In these studies, the wave forces and hydrodynamic coefficients were reported. Focusing on the improved performance of FBWs, Cho (2016) examined the transmission coefficient changes in a long rectangular floating breakwater by adding porous side plates. To determine the effect of a stepped topography, Guo et al. (2016) investigated oblique wave scattering by a semi-infinite elastic plate. They extracted some parameters such as transmission and reflection coefficients, energy conservation, and moment for the plate, which are useful in engineering designs. However, in some cases, the length of these floating structures is limited. In these cases, radiation and diffraction problems should be considered and analyzed in a three-dimensional (3D) manner. Kao et al. (2015) developed a 3D model to investigate wave-floating structure interaction. The results indicated the model capability for the computation in an open sea.

Another classification is related to the selection of numerical methods. Taking the dynamic behavior of floating structures into account, some researchers implemented the finite element method (FEM) to simulate the wave-structure interaction problem (Turnbull et al., 2003; Sannasiraj et al., 2001; Taylor and Zietsman, 1981). These researches significantly emphasized on how to model the radiation boundary in an unbounded solution domain. Another series of research belongs to the boundary element method (BEM) (Chen and Mahrenholtz, 1992; Kao et al. 2015; Au and Brebbia, 1983, Ryu et al., 2003, Kaligatla and Manam, 2014). The critical point to note in the BEM-based studies is to determine the fundamental solution and solve the singular points. Over the last two decades, combining the advantages of two above-mentioned numerical methods, a novel numerical method, namely the scaled boundary finite element method (SBFEM) has been employed to investigate various Engineering problems, including heat conduction problem (Bazyar and Talebi, 2015; Mohasseb et al., 2017), hydraulic fracture (Zhong et al., 2018), water wave-structure interaction (Li et al., 2013b). By considering various cross-sections for the bottom-mounted cylindrical structures, Tao et al. (2007), Tao et al. (2009), Song and Tao (2010), Li et al. (2013a), Meng and Zou (2012) and Liu and Lin (2013) conducted researches on the wave diffraction problem. In these investigations, the standard scaled boundary coordinate system applied for both bounded and unbounded sub-domains. In the standard coordinate system, a so-called scaling center should be considered. It was shown that the SBFEM is an efficient method even by a few numbers of elements. Li et al. (2005a, 2005b) developed the original SBFEM by creating a new local coordinate system for the media with parallel side-faces. They employed the modified and standard SBFEM coordinate system to solve the wave radiation and diffraction problems in some two-dimensional cases. Song and Tao (2011) researched the issue of wave interaction with a horizontal elliptic cylinder according to the coordinate systems proposed by Li et al. (2005a, 2005b). They concluded that the SBFEM does not suffer from some serious drawbacks, such as difficulties caused by irregular frequencies and sharp corners. More recent studies (Meng and Zou, 2013) investigated the wave radiation and diffraction problems by a two-dimensional floating structure close to a sidewall. In three previous reviewed studies, the scaling center selected on the body surface for bounded sub-domains. Although this selection leads to obtaining the analytical distribution of the velocity potential on the body boundaries, the governing equation becomes non-homogeneous. Therefore, a particular solution or other techniques should be employed.

Although a large number of numerical models have been devoted to the 2DV analysis of wave diffraction problems, the effects of the "wave diffraction around the breakwater" have remained unexplored. These effects are caused by wave turning around the structure, toward the area that is more sheltered against the waves. In practice, this effect cannot be ignored- especially in cases where FBWs have a finite length. In such cases, 2DV modeling would not yield

accurate results. Because of the phase difference between transmitted waves beneath the structure and the diffracted waves around the breakwater, these waves can amplify or cancel each other in the shadow region. This complexity can only be explained and estimated by a full 3D model. However, the 3D analysis gives rise to computational costs. To avoid the 3D modeling, the main purpose of this paper is to develop an efficient 2DV model and a set of predictive correction factors to make the 2DV results comparable with 3D results and thus increase the accuracy of 2DV predictions. The predictive model is an Artificial Neural Network (ANN) in which trained via a database. This database contains both 2DV and 3D results for various cases obtained from the changes in the characteristics of model geometry and frequencies of incident waves. Figure 1 shows the procedure of applying this method in the current study.

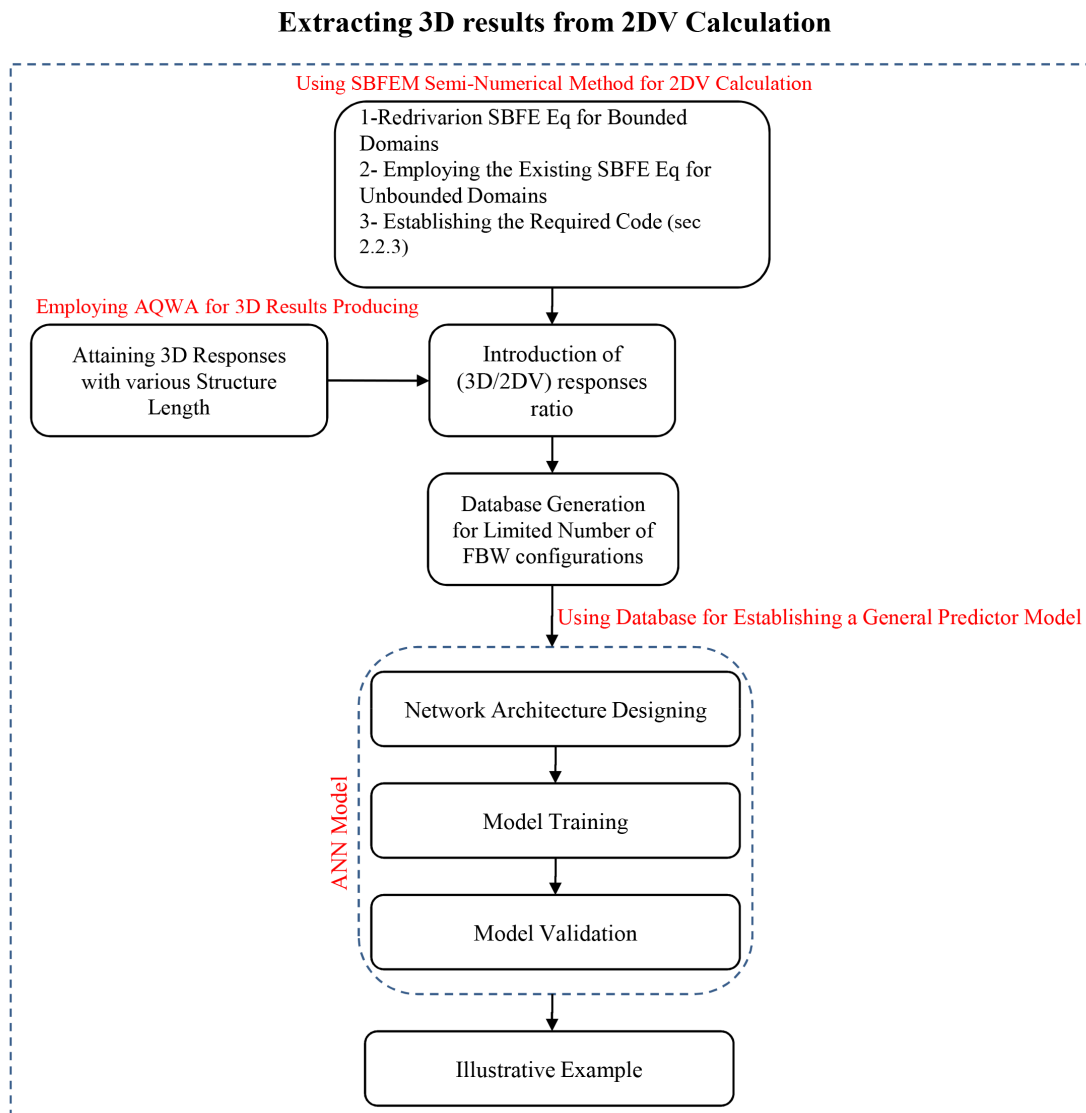


Figure 1 Procedure of applying proposed method

First of all, in the 2DV model, unlike the studies of Li et al. (2005a), the scaling center of bounded sub-domains is located within the solution domain. This decision leads to employing numerical integration to calculate the hydrodynamic forces exerted on the structure. Also, in the cases where the normal velocity exists on any boundary of the sub-domains, the governing equation becomes homogeneous in the scaled boundary coordinate system. Thus, by eliminating the need for various particular solutions, various problems of wave-floating structure interaction can be solved in a unified manner. The code for generating 2DV results is developed by using the derived equations for the bounded sub-domains and the existing SBFEM equations for unbounded media.

Second, because of the similarity of governing equation to the 2DV model, the ANSYS AQWA software is used to provide the 3D results. For each sample case, the obtained 3D responses (transmitted coefficient, TC) are divided into the 2DV ones. The result of this division is called the ' $\frac{TC_{3D}}{TC_{2D}}$ ratio' in this study.

Finally, by utilizing the generated database an Artificial Neural Network is designed. The duty of this predictor model is to anticipate mentioned ratio as a "corrector factor" for new cases. For a structure with arbitrary length, by applying anticipated factors, 2DV results convert to 3D results along the centerline perpendicular to FBWs.

2 Two dimensional modeling

2.1 Governing equations

As demonstrated in Figure 2, the problem of linear wave scattering by a rectangular floating body is considered in the present study. The floating structure is assumed to be fixed in place. The width and draft of the structure are B and T , respectively, and the water depth is H . The $o - xyz$ Cartesian coordinate system is obtained to map $o - xy$ plane on the undisturbed free surface, where z axis is directed upward.

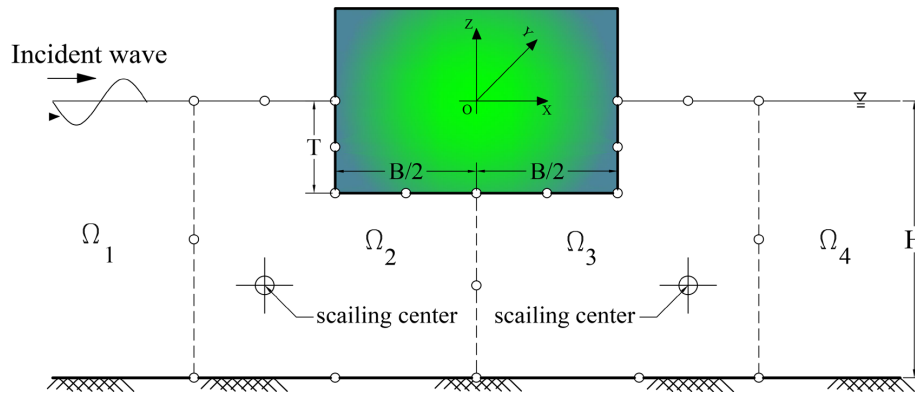


Figure 2 Definition sketch of wave diffraction for a rectangular structure in infinite fluid domain

By assuming an ideal fluid, the irrotational flow field can be described by velocity potential. By separating variables for periodic wave motion, the velocity potential is described as:

$$(1) \Phi(x, z, t) = \text{Real}\{\phi(x, z)e^{-i\omega t}\}$$

Where ω is the wave angular frequency, which is related to the wavenumber k by the dispersion relation $\omega^2 = gk \cdot \tanh(kH)$ and g is the gravitational acceleration. For an irrotational flow, ϕ satisfies the Laplace equation:

$$(2) \nabla^2 \phi = 0$$

The boundary conditions can be expressed as follows:

$$(3) \frac{\partial \phi}{\partial z} = \frac{\omega^2}{g} \phi, \text{ on the water free surface } (z = 0)$$

$$(4) \frac{\partial \phi}{\partial z} = 0, \text{ on the bottom } (z = -H)$$

$$(5) \frac{\partial \phi}{\partial n} = \bar{v}_n, \text{ on a solid surface}$$

In this study, \bar{v}_n is used to refer to the known normal velocity. On the infinite boundaries, Sommerfeld boundary condition is applied:

(6) ϕ : outgoing, finite value on Γ_∞

2.2 Scaled Boundary Finite Element Method

2.2.1 Formulation for bounded medium

The main characteristics of SBFEM used in the present paper are described in this section. The detailed implementation of SBFEM for hydrodynamic problems can be found in Li et al. (2005a).

The original scaled boundary coordinate system is based on describing a domain by scaling its boundary (S) relative to a scaling center (x_0, y_0). The scaling center should be selected in the region where the whole boundary of the sub-domain can be directly visible. The solution domain should be divided into some smaller sub-domains to apply SBFEM to a region where such point does not exist. By this subdividing, the scaling center is retrieved for each solution domain. A scaled boundary coordinate system is described by two coordinates (ξ, s), as shown in Figure 3. The circumferential coordinate (s), which measures the distance counterclockwise, is defined along the curve S . Moreover, the normalized radial coordinate ξ is one on the curve S and zero at the scaling center. Therefore, each ξ less than unity illustrates a version of the boundary. It should be noted that the side-faces ($s = s_0, s = s_1$) meet where the curve S is closed. Therefore, it can be concluded that the entire domain in this system is described by $0 \leq \xi \leq 1, s_0 \leq s \leq s_1$.

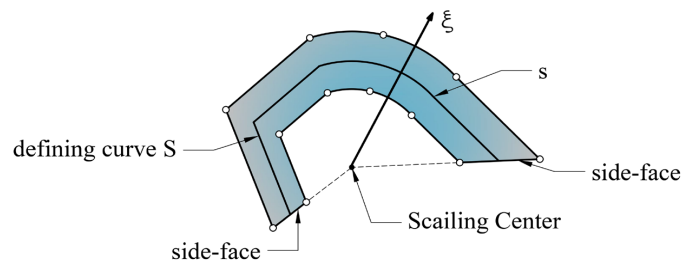


Figure 3 Standard coordinate system for SBFEM

As shown in Figure 2, the entire fluid domain is divided into N sub-domains, shown by Ω_n ($n = 1, \dots, N$). This division is led to the creation of j common interfaces, $\Gamma_{int,j}$ ($j = 1, \dots, N - 1$), between the sub-domains and i other boundaries, $\Gamma_{bn,i}$, in each sub-domains (Figure 4). The unbounded sub-domains are limited by $\Gamma_{int,1}$ or $\Gamma_{int,N-1}$ in one side and Γ_∞ on the other side.

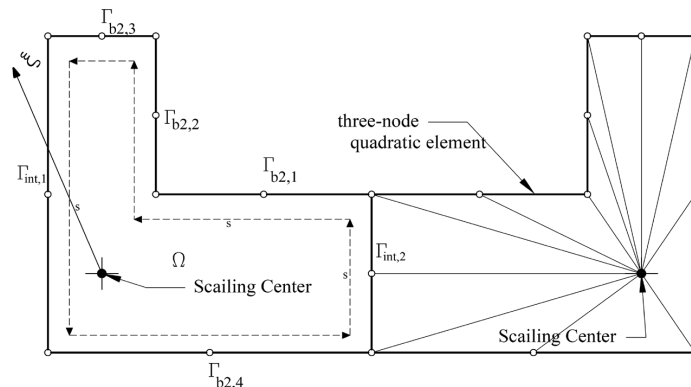


Figure 4 Discretization of domain boundaries for bounded sub-domains

The mapping in SBFEM is consistent with the isoperimetric element formulation in the classical FEM. Thus, by arranging nodal coordinates of an element in the form of two vectors $\{x\}$ and $\{y\}$, the coordinate of an arbitrary point on the element can be approximated through the nodal coordinates. Moreover, the coordinate of a point within the domain can be described based on scaling the boundary by normal coordinate. Hence, the Cartesian coordinate can be related to the scaled boundary coordinate system as follows:

$$(7) \hat{x} = x_0 + \xi[N(s)]\{x\}$$

$$(8) \hat{y} = y_0 + \xi[N(s)]\{y\}$$

Where (\hat{x}, \hat{y}) and (x_0, y_0) are the points within the domain and scaling center coordinate, respectively. For an element, the approximated value of potential in the circumferential direction can be written as:

$$(9) \phi(\xi, s) = [N(s)]\{a(\xi)\}$$

$\{a(\xi)\}$ is defined as the potential function in radial direction passing through the scaling center and a node on the boundary, and $[N(s)]$ is the shape function. Unlike the studies of Li et al. (2005a) and Meng and Zou (2013), the scaling center is considered within the sub-domains in this study. This decision leads to the elimination of the effects of side-faces. In other words, this will make the governing equation homogeneous even if there exist some velocity vectors normal to the body boundaries. Therefore, there is no need to consider a particular solution or other methods to solve the problem. So, the SBFEM equations in terms of the potential function $\{a(\xi)\}$ and the nodal flow function $\{q(\xi)\}$ on the domain boundary can be expressed as:

$$(10) [E_0]\xi^2\{a(\xi)\}_{,\xi\xi} + ([E_0] + [E_1]^T - [E_1])\xi\{a(\xi)\}_{,\xi} - [E_2]\{a(\xi)\} = 0$$

$$(11) \{q(\xi)\} = [E_0]\xi\{a(\xi)\}_{,\xi} + [E_1]^T\{a(\xi)\}$$

Where $[E_0], [E_1], [E_2]$ and $[M]$ are formed by assembling the element coefficient matrices.

2.2.2 Applying scaled boundary finite element method to a semi-infinite medium

It is necessary for the numerical modeling of wave-structure interaction to determine the effect of the far-field fluid boundary. The effect of the semi-infinite fluid domain can be efficiently calculated using the SBFEM. For this purpose, a single curve called the 'defining curve' should be discretized, as shown in Figure 5. By defining the radial coordinate in the horizontal direction, the unknown nodal potential function $\{a(\xi)\}$ is defined along the radiation direction. Therefore, the SBFEM equation in terms of $\{a(\xi)\}$ and $\{q(\xi)\}$ can be written as:

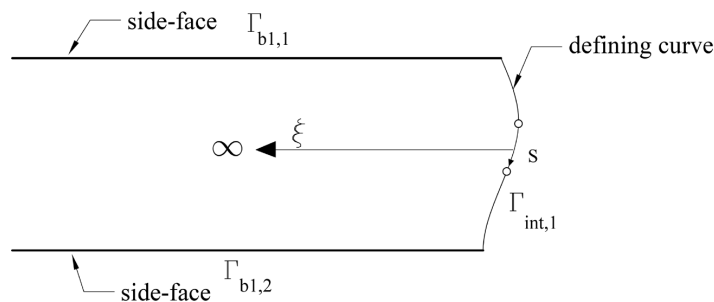


Figure 5 Applying SBFEM for semi-infinite sub-domains with parallel side-faces

$$(12) [E_0]\{a(\xi)\}_{,\xi\xi} + ([E_1]^T - [E_1])\{a(\xi)\}_{,\xi} + (\bar{k}^2[M_0] - [E_2])\{a(\xi)\} = 0$$

$$(13) \{q(\xi)\} = [E_0]\{a(\xi)\}_{,\xi} + [E_1]^T\{a(\xi)\}$$

2.2.3 Solution process

In this study, a code is developed to solve Equations (10) to (13). This program intends to evaluate the potential values in the fluid domain. The hydrodynamic pressure exerted on the structure, and the amplitude of the transmitted and reflected waves are calculated based on evaluated potentials values. The inputs of the program include the coordinates of the nodes in each sub-domain, characteristics of the incident wave, fluid properties, and the element type to discretize the solution domain. The procedure of the solution is presented in Figure 6.

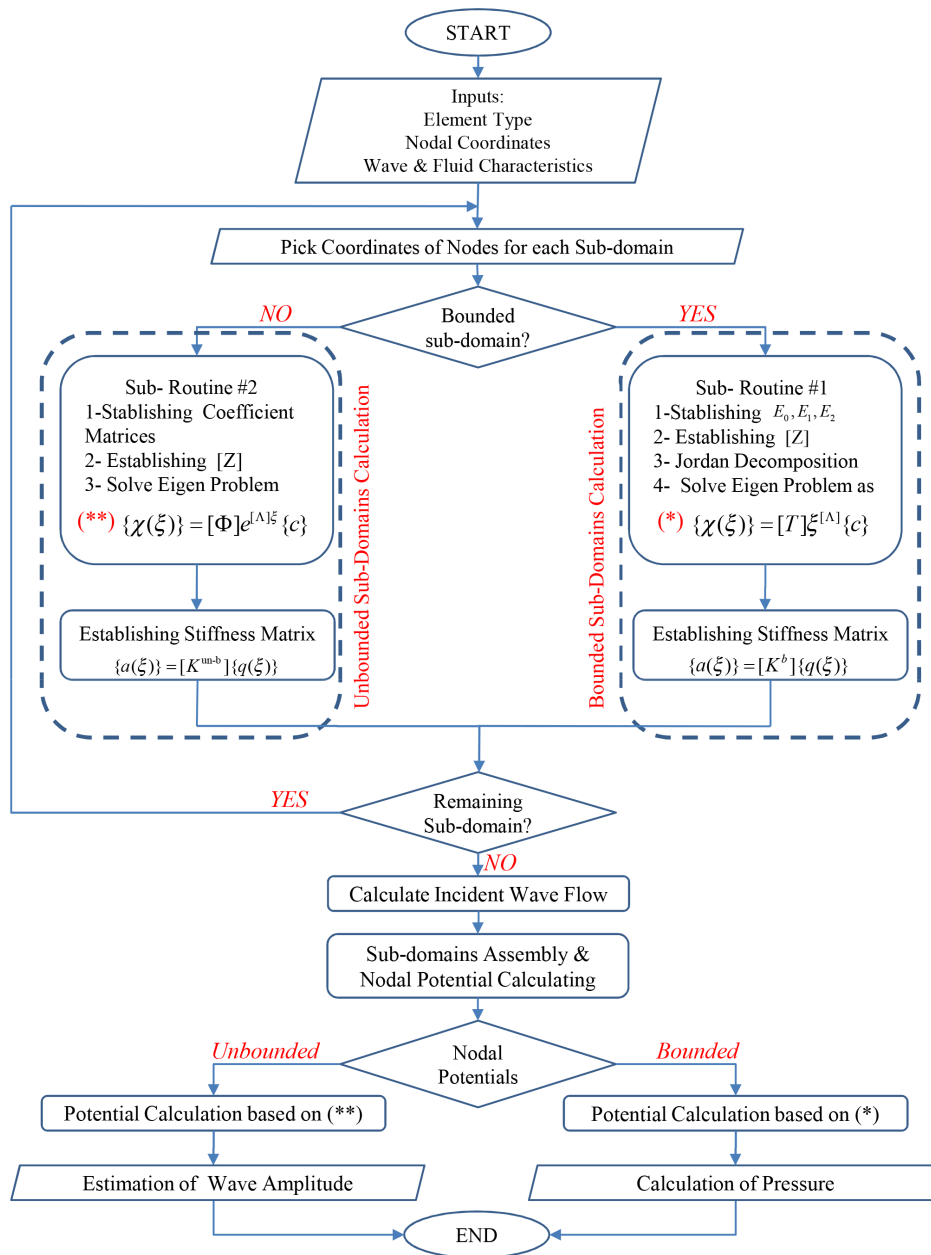


Figure 6 The procedure of SBFEM for 2DV analysis

By obtaining the coordinates of the nodes in each sub-domain, the coefficient matrices $[E_0], [E_1], [E_2]$ are first calculated. By introducing a new variable $\{\chi(\xi)\} = \begin{Bmatrix} a(\xi) \\ q(\xi) \end{Bmatrix}$, Equations (10) and (12) are transformed from second-order differential equations into the systems of ordinary first-order differential equation. The complete procedure of solving the Eigen-value problems for the bounded and unbounded sub-domains is given in Appendices A and B. By establishing the general solution in each sub-domain, the relationship between the nodal potential and the nodal flows, which is considered as the stiffness matrix, is extracted. Evaluating the nodal flow induced by the incident potential and considering the matching boundary conditions at the interface of adjacent sub-domains, the stiffness matrices are assembled. The assembled stiffness matrices create a system of equations where its solutions are the nodal potential values. By returning the nodal potential values to Equations (*) and (**) in Figure 6, the integral constants and potential functions are obtained in each sub-domain. Based on estimated potential, the values of pressure and amplitude of the transmitted and reflected waves can be calculated.

2.2.4 Model validation

In order to verify the current SBFEM-based model, a specific case in the numerical investigation of Zheng et al. (2004b) is addressed. In this section, the computational results of the vertical and horizontal excitation wave forces are compared with the reported results. The results of the wave diffraction problem by a rectangular breakwater in an infinite fluid domain with finite water depth are considered. The geometric parameters, in this case, are $H/B = 1$ and $T/H = 1/3$. According to Li et al. (2005b), the accuracy of computational results is well consistent with few elements. Thus, as shown in Figure 2, two three-node quadratic elements are used to discretize each boundary. Therefore, 12 and 2 elements are considered to discretize the bounded and unbounded sub-domains, respectively. The wave force in k direction can be expressed as:

$$(14) F_{wk} = i\omega\rho \int_{s_0} (\phi_I + \phi_D)n_k ds$$

Where ρ is the water density, s_0 is the wetted surface of body in XOZ plane and n_j is the generalized normal unit vector with $n_1 = n_z$ and $n_2 = n_x$ for the vertical and horizontal forces, respectively. For each bounded sub-domain, there are 5 nodes belong to two elements on the structure boundaries. The Newton-Cotes rule is employed to calculate these integrals. The dimensionless wave force is defined as:

$$(15) F_k = |F_{wk}| / (\rho g A B) \quad ; k = 1, 2$$

Where A is the amplitude of the incident wave. Figure 7 shows the dimensionless wave force in two directions versus KT .

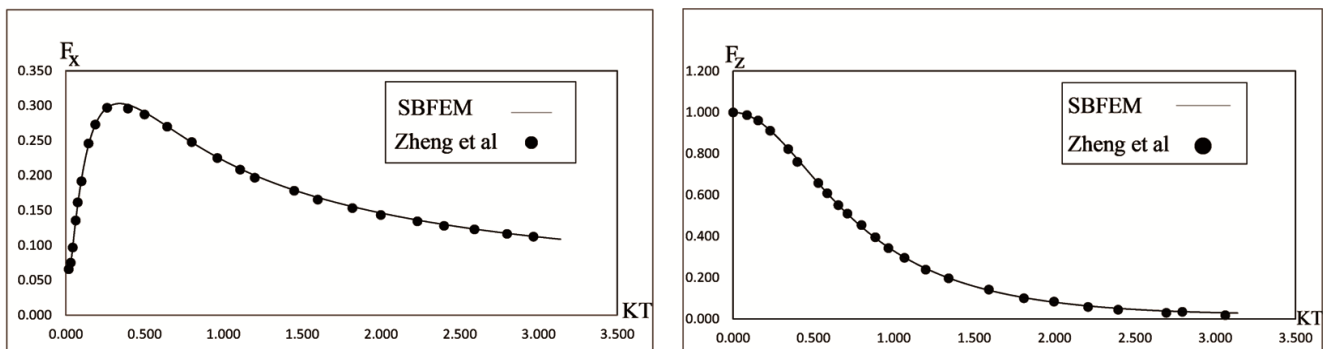


Figure 7 Wave forces on rectangular structure in infinite fluid domain

The results presented in Figure 7 are indications of valid results of the SBFEM presented in this paper.

3 Three-dimensional modeling by ANSYS AQWA

ANSYS AQWA can be employed to examine the diffraction theory around three-dimensional floating rigid bodies. The static and dynamic analyses can be performed with it to calculate the pressure on the floating structures and their mutual responses.

AQWA is based on the 3D panel method. Using the principal of Green’s integral theorem, the Laplace equation is transformed into a two-dimensional integral equation on the body surface. With regard to this transformation, the structure surface is meshed by a limited number of two-dimensional panels to solve the integral numerically. Moreover, the fluid free surface is modeled by two-dimensional grids. The integral obtained by Green’s theory represents several sources or sinks and dipoles on the surface (Journee, 2001). The Superposition of the flow elements yields the potential values at grid points. By interpolating between the grid points, the velocity potential of an arbitrary point on the free surface can be calculated. Nonlinear effects such as drift and second-order Stokes waves are disregarded in the present study.

Along the centerline perpendicular to object, by increasing the length of structures, the effects of diffracted waves around the FBWs on transmitted waves beneath the body will be decreased. According to Holthuijsen (2010), for the bottom-mounted breakwaters with the length more than ten times the incident wavelength, the effect of this phenomenon will be minimized in the centerline. This finding is used to verify the extracted results by AQWA. So, a breakwater with a width and draft of $12m$ and $2m$, respectively, in water with the depth of $6m$ is considered against a linear wave with the period of $4s$. The calculated transmitted and reflected wave amplitudes by AQWA is compared with 2DV modeling results. In the 3D models, the lengths of the simulated structures are assumed to be 40 , 100 and $300m$. According to software requirements, the maximum element size is determined by the maximum wave frequency and is chosen to be $0.75m$. By inspection, it is concluded that as long as this requirement is fulfilled, the accuracy of transmitted and reflected coefficient results does not change for element sizes smaller than the mentioned maximum value. The results of these 3D models are compared with 2DV ones in Figure 8.

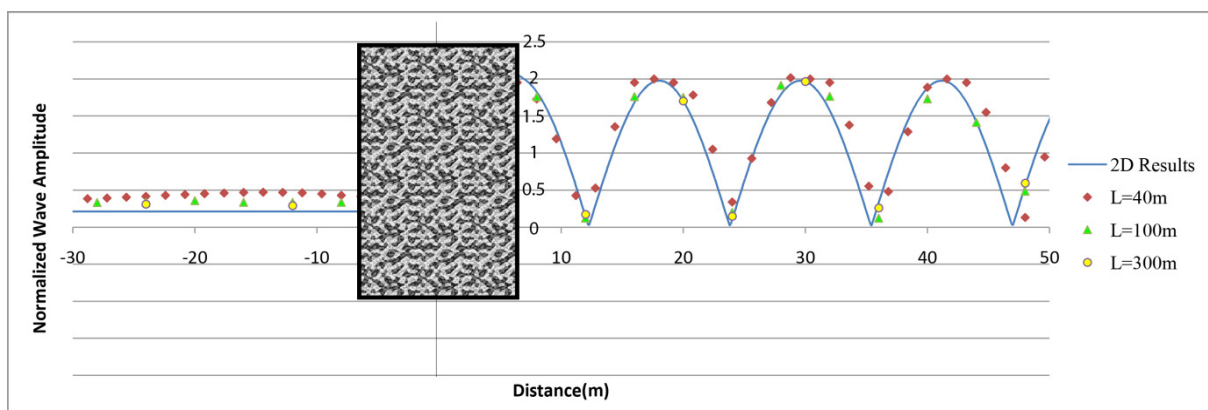


Figure 8 Comparison of 2DV modeling results with 3D ones for different length of structures

The horizontal axis of this chart demonstrates the distance of the different points from the structure, and the vertical axis is the amplitude of the transmitted and reflected waves over the incident wave amplitude. As illustrated in Figure 8, since the incident wavelength is $21.13m$, as expected, the 3D diffraction effects for the structure with the length of $300m$ is minimized. This finding can also demonstrate the AQWA modeling validation. It is also observed that by decreasing the structure length, the difference between the 2DV modeling and 3D modeling results is increased. In the next step, by using the validated 2DV and 3D models, a database is created for the design of the ANN model.

4 Ratio of two-dimensional to three-dimensional response

To create a dataset for the ANN analysis, the breakwater length, X , the body width, B , the draft of structure, T , and the incident wavelength, L , are used as input variables to generate various sample cases. Four input parameters with three different values create 3^4 combinations in the 3D analysis. Similarly, 27 cases in the 2DV model are simulated.

The different values of the mentioned parameters are shown in Figure 9. The ANN toolbox in MATLAB is employed to carry out the calculations. 74 out of 81 three-dimensional cases are derived randomly to train this model. After the training, the developed network validation is checked through 7 remaining cases.

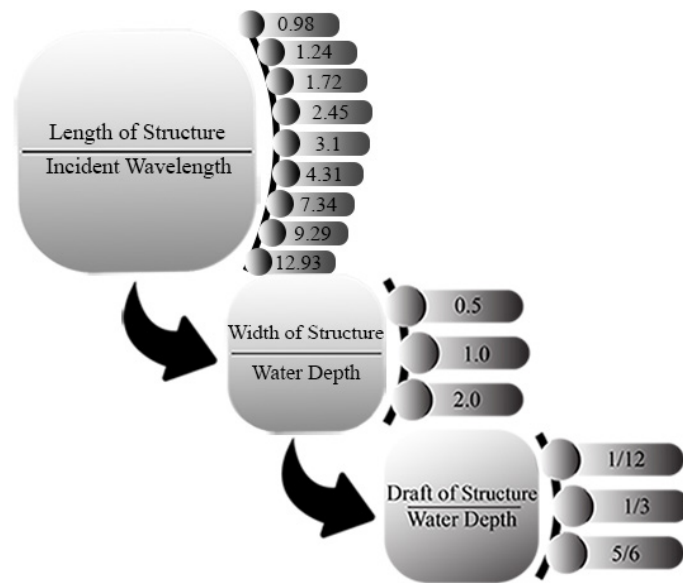


Figure 9: Parameters of 3D created models

To calculate the transmission coefficient, similar to Koutandos et al. (2005), the transmitted wave amplitude is measured at the point in the center line perpendicular to the breakwater at half of the incident wavelength from the structure.

4.1 Artificial neural network (ANN)

ANN method based on backpropagation learning algorithm has been employed in the present study. By adjusting various internal weights and biases during the network training, it is expected from the designed network to meet its target by minimizing the mean square error between the actual and the predicted vectors. This minimization is done by the gradient search technique. An appropriately trained neural network can accurately predict the outputs even for the inputs not used in the network training (Dhara et al., 2008).

In this study, the input vectors of ANN include the dimensionless parameters X/L , B/H and T/H which are used in the normalized form. The network target is ' $\frac{TC_{3D}}{TC_{2D}}$ ratio'. Among all the training algorithms, the Levenberg–Marquardt

(LM) is considered, which is one of the fastest and most efficient algorithms. The number of neurons in the input and output layer is set to 3 and 1, respectively. Determining the number of hidden layers and neurons in each hidden layer is an important criterion for the design of the neural network structure (Seibi and Al-Alawi, 1997). According to Fausett (1994), the back-propagation architecture is sufficient with one hidden layer for most applications; therefore, only one hidden layer is considered. Seibi and Al-Alawi (1997) suggested the following formula to calculate the number of neurons for a single hidden layer if the number of training pairs is known:

$$(16) \quad n = \theta \times (N_h \times (m + 1) + p \times (N_h + 1))$$

Where n is the number of possible training pairs, θ is a constant coefficient greater than one, N_h is the number of neurons in hidden layer which are used in the network with a hidden layer, and m and p express the number of input and output nodes, respectively. Using the above formula N_h will be 7.97, and hence, 8 neurons are considered. The architecture of the neural network is introduced in Figure 10.

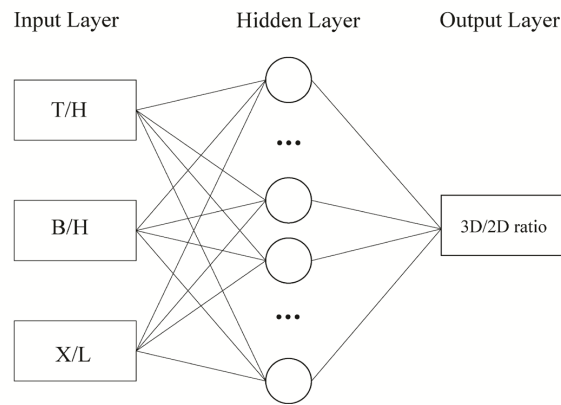


Figure 10 Architecture of designed neural network

4.2 Evaluation of developed model

In the previous section, the architecture of the considered neural network model is described. Anticipating the ratio of 3D to the 2DV responses for the transmission coefficient - $\frac{TC_{3D}}{TC_{2D}}$ ratio - is the main duty of the designed ANN model.

In other words, by evaluating the 2DV results via the SBFEM method and utilizing the mentioned ratios, predicted by the trained ANN model, the 3D responses can be approximated. After regulating the network framework, in this section, the target and predicted values are compared to estimate the accuracy of the trained model. Eventually, to evaluate the performance of the trained model against the new cases, the predicted results are compared with the targets for the 7 cases, which are not be used for the training process.

The Correlation Factor (R) and the Mean Squared Error (MSE) of the target and predicted values for the data used in the “training” of the ANN model are 0.93 and 0.079 , respectively. Figure 11 compares these two series of data. In order to calculate the data dispersion rate, the Coefficient of Variations ($C.V$) for the mentioned ratio, between the target and the predicted values, is 0.194 . These criteria indicate the accurate results of the designed neural network model and the marginal and controlled dispersion of the predicted values relative to the expected values.

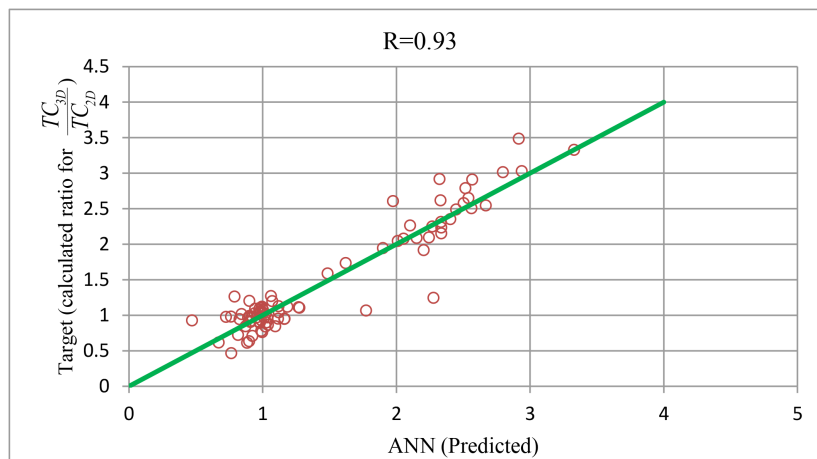


Figure 11 Dispersion of target and predicted values for datasets used in training process

Moreover, to determine the model's performance, the effects of principal parameters variation on the target and predicted values are investigated. Initially, the effects of changes in T/H on ' $\frac{TC_{3D}}{TC_{2D}}$ ratio' for both the target and the predicted values are studied. In this comparison, some datasets with constant values of $B/H = 0.5$ and $X/L = 12.93$, and the variable values of T/H are derived. As shown in Figure 12, with the increase in the draft of structure, T/H , the difference between the 3D and 2DV responses grows as well. This observation can be interpreted as by increasing the

structure draft; fewer waves can pass beneath the structure. Therefore, in the 2DV model, most of the wave energy is reflected. However, in the 3D model, the waves can turn around the object toward the shadow region; thus the 2DV and 3D responses diverge from each other. It is observed that the ANN model has correctly predicted this phenomenon. The very slight differences between the predicted and the target values are related to the approximated inference of artificial intelligence methods in Engineering. It should be noted that for this part of the studied data, CV is 0.034 , which indicates the accuracy of the trained model to anticipate target values.

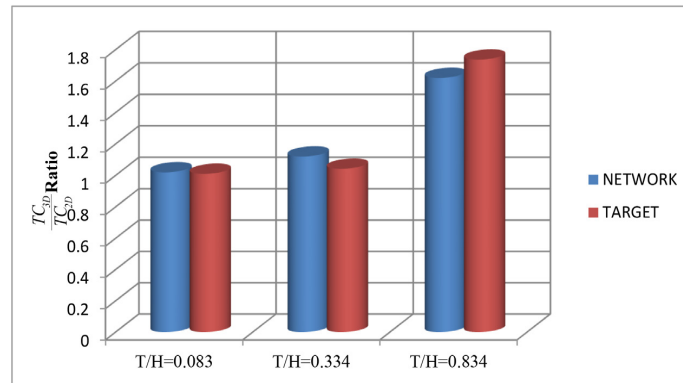


Figure 12 Effect of T/H variations on target and predicted values

Also, in another effort, as shown in Figure 13, the effect of the X/L variations on the $\frac{TC_{3D}}{TC_{2D}}$ ratios - for both expected and predicted values - is investigated. This comparison is made for the cases with the constant values of $B/H = 0.5$ and $T/H = 0.084$.

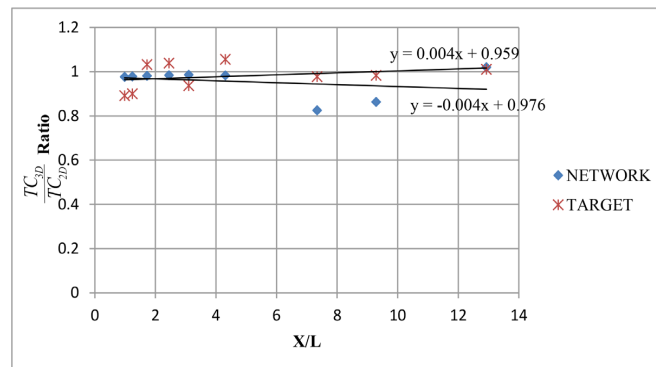


Figure 13 Effect of X/L variations on target and predicted values

For this comparison, the small values of B/H and T/H are selected. These selections allow most of the wave energy to pass beneath the structure. Therefore, it is expected that the waves in the shadow region be mainly due to the passing waves. This reason explains why the coefficient ' $\frac{TC_{3D}}{TC_{2D}}$ ratio' is about unity. It can be seen that the network correctly predicted this phenomenon. Besides, it is seen that the network has higher prediction accuracy in computational cases with $0.0 < X/L < 5.0$. Because of a higher number of cases with X/L in this range (according to Figure 9, 54 out of 81 datasets), this higher accuracy can be justified. Moreover, it is observed that the neural network underestimates the targets for $X/L > 5.0$ (in fact, the higher number of the data for $X/L < 5.0$ affects the prediction accuracy for $X/L > 5.0$). In this comparison, the Coefficient of Variations is 0.092 , which still indicates the high accuracy of the predicted values.

Finally, the effect of the B/H variations on the ' $\frac{TC_{3D}}{TC_{2D}}$ ratio' for target and predicted values is investigated. The values of this ratio for $T/H = 0.0834$ and $X/L = 2.45$, per various B/H , are shown in Figure 14. Considering the small structure draft value ($T/H = 0.0834$) facilitates the possibility of the wave passing beneath the structure - rather than being diffracted around the structure -. Thus, the results of the 2DV and 3D model converge, and their responses ratio is about unity. By increasing the width of the structure, the possibility of the waves passing beneath the structure will reduce. Therefore, the effect of the waves diffracted around the structure is more noticeable in the shadow region, and the 3D results diverge from the 2DV ones. In this case, $C.V = 0.034$.

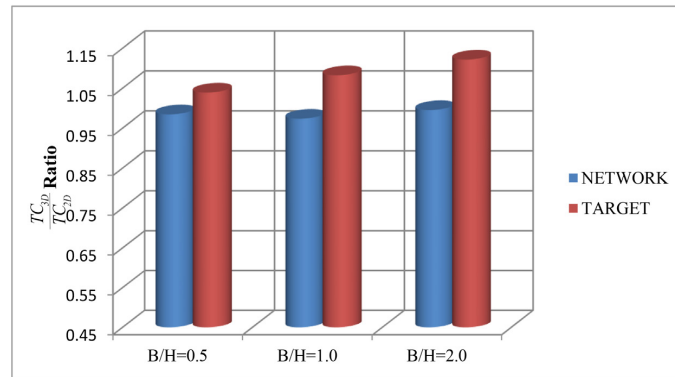


Figure 14 Effect of B/H variations on target and predicted values

As another evaluation method, the performance of the trained ANN model against new cases is examined for around 10% of the datasets (7 series of datasets), which are not be used in the network training process. The characteristics of the datasets and the values of the target and predicted ratios are shown in Table 1. The second, third, and fourth columns of this table represent the "normalized" form of B/H , T/H and X/L , respectively. The values of the target ratio are also shown in the fifth column. The sixth column shows the ratio values predicted by the ANN model. With this regard, the minimum and maximum differences between target and predicted values are about 2% and 12%, respectively.

Table 1 Comparison of target and predicted values for $\frac{TC_{3D}}{TC_{2D}}$ ratio (the values of the variables are normalized)

Test No	B/H	T/H	X/L	TARGET Values	Predicted Values (ANN)
1	0.25	0.1	0.333333333	1.0555	0.9665
2	0.5	0.1	0.718484145	0.9766	0.9543
3	1	0.1	0.56767208	0.9463	0.8628
4	0.25	0.4	0.239752514	0.9696	1.0397
5	0.5	0.4	0.56767208	0.9502	1.0474
6	0.25	1	0.239752514	1.9190	2.1884
7	1	1	0.718484145	1.5879	1.4524

As can be seen in the selected cases, except for cases 6 and 7, the obtained 2DV and 3D response values are very close and the ' $\frac{TC_{3D}}{TC_{2D}}$ ratio' is about unity. However, the difference between the 2DV and 3D responses are significant for cases 6 and 7. As mentioned previously, the reason for this difference is due to the high draft of the structure. In case 7, the 3D results are more than 50% higher than the 2DV ones. Also, the difference between the responses in case

6 is about 100%. It's seen, the trained ANN model well predicted these differences. Moreover, for a constant value of $T/H = 0.1$ in the first three cases, - regardless of the changes in X/L - it is evident that the 2DV results slowly diverge from the 3D responses by increasing the B/H , which the ANN model correctly estimated the downward trend. In contrast, although the target and predicted values in cases 4 and 5 are close together, the neural network anticipated the mentioned ratios slightly lower than the target values. To better illustrate the relationship between the target and the predicted values, the data presented in Table 1 are shown in Figure 15. It is observed that the designed neural networks can predict the results for new datasets with good accuracy. The Coefficient of Variations between the target and the predicted values is 0.099 .

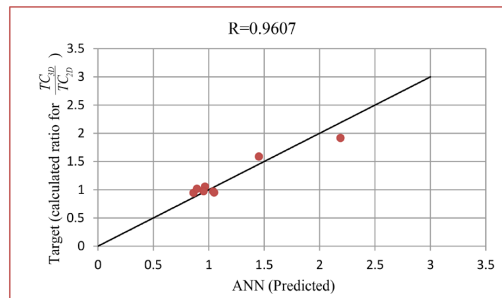


Figure 15 Dispersion of target and predicted values for new datasets

5 Illustrative examples

The results of the model, which are shown in Figure 8 are considered again to clarify the performance of the correction factor in converting the 2DV results into the 3D responses. By applying the predicted factor of trained ANN to the 2DV results, the 3D responses are predicted for the structures with 40, 100 and 300m length. The results are shown in Figure 16. It is observed that by applying the mentioned factor, the 2DV modified results are very close to the 3D modeling results.

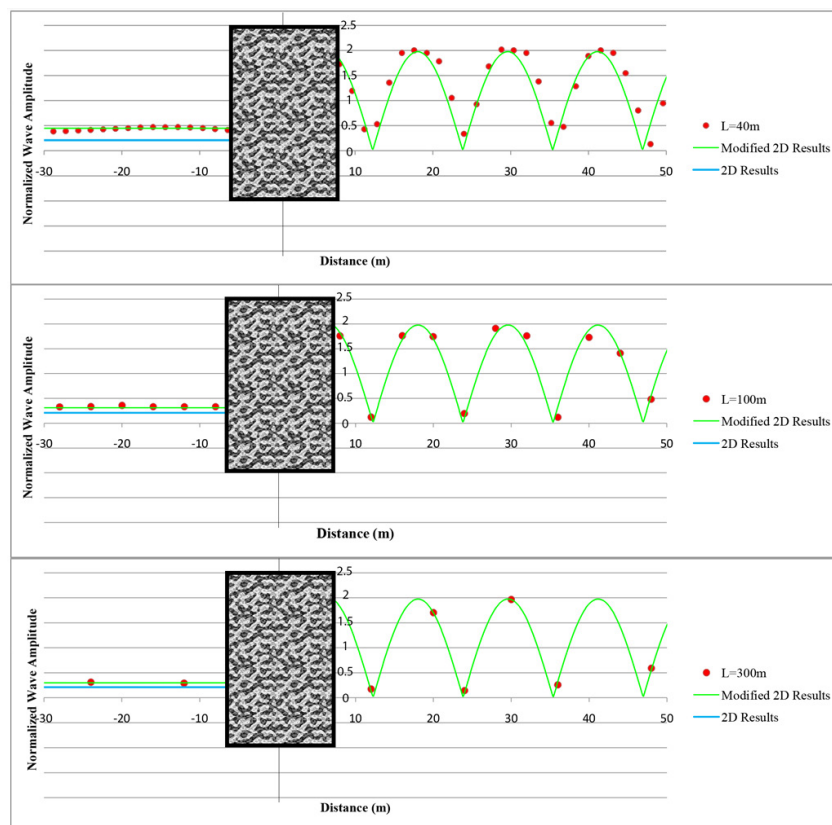


Figure 16 Comparison of 2DV modeling results with 3D ones for different length of structures

The results of this study indicate that the proposed method brings notable benefits for predicting the 3D response of the FBW with an arbitrary length. Due to applying a 2DV model in the case of 3D phenomena, the computational effort becomes cost-effective. In order to show the efficiency, 10 of the sample cases are solved by both the 2DV-ANN combination model and AQWA model. About 500% of time saving are obtained by employing the combined model.

6 CONCLUSION

SBFEM method is used as a powerful semi-analytical method to solve the diffraction problem in the case of the fixed objects in the infinite fluid domain. Detection of a correction factor to extend the result of 3D solutions from the 2D analysis has been the main purpose of the current study. A database of 81 different cases in geometry and wave frequency is established, and ANN is designed to give the correction factor. The code is written to solve 2D cases using SBFEM. The ANSYS AQWA numerical software is used for 3D solutions. The following development and results are notable:

1. The center of SBFEM is moved from the corner of the floating object to the middle of the bounded sub-domains. This change will allow the user to use an arbitrary mesh on the structure boundaries.
2. Comparing the results of the present 2DV code with other numerical and analytical studies shows an excellent agreement to verify the code.
3. It is shown that the semi-analytical solution (SBFEM) is exact in the radial direction and can evaluate the potential at any given point independent of the numerical mesh.

It is shown that the designed artificial neural network is able to estimate the result of 3D cases - along the centerline perpendicular to the structure - by the 2DV model. The correlation factor $R = 0.9607$ for a group of new samples shows the predicted results are closely matched to the target values.

The proposed combined model is shown to be accurate, rapid, and efficient. For 10 of the sample cases, by comparing the needed time of solving, it is obtained that the 2DV-ANN combined model is around 500% faster than ANSYS AQWA's run-time.

Acknowledgement

The authors would like to thank Dr.Sassan Mohasseb for providing technical supports and valuable suggestions in every stage of this work.

Author's Contributions: Investigation and Writing, M Qorbani Fouladi; Supervisions, P Badiei and Sh Vahdani.

Editor: Pablo Andrés Muñoz Rojas.

References

- Abbasnia, A., & Ghiasi, M. (2014). Nonlinear wave transmission and pressure on the fixed truncated breakwater using NURBS numerical wave tank. *Latin American Journal of Solids and Structures*, 11(1), 51–74.
- Abul-Azm, A. G., & Gesraha, M. R. (2000). Approximation to the hydrodynamics of floating pontoons under oblique waves. *Ocean Engineering*, 27(4), 365–384.
- Au, M. C., & Brebbia, C. A. (1983). Diffraction of water waves for vertical cylinders using boundary elements. *Applied Mathematical Modelling*, 7(2), 106–114.
- Bazyar, M. H., & Talebi, A. (2015). Scaled boundary finite-element method for solving non-homogeneous anisotropic heat conduction problems. *Applied Mathematical Modelling*, 39(23-24), 7583-7599.
- Chen, S., & Mahrenholtz, O. (1992). *Interaction of water waves and floating twin cylinders in beam waves*.
- Cho, I. H. (2016). Transmission coefficients of a floating rectangular breakwater with porous side plates. *International Journal of Naval Architecture and Ocean Engineering*, 8(1), 53–65.

- Dhara, S. K., Kuar, A. S., & Mitra, S. (2008). An artificial neural network approach on parametric optimization of laser micro-machining of die-steel. *International Journal of Advanced Manufacturing Technology*, 39(1–2), 39–46.
- Fausett, L. (1994). *Fundamentals of neural networks: architectures, algorithms, and applications*. Prentice-Hall, Inc.
- Guo, Y., Liu, Y., & Meng, X. (2016). Oblique wave scattering by a semi-infinite elastic plate with finite draft floating on a step topography. *Acta Oceanologica Sinica*, 35(7), 113–121.
- Holthuijsen, L. H. (2010). *Waves in oceanic and coastal waters*. Cambridge university press.
- Journee, J. M. J. (2001). Journee, J, MJ and Massie, WW Offshore Hydrodynamics. *Delft University of Technology*.
- Kaligatla, R. B., & Manam, S. R. (2014). Flexural gravity wave scattering by a nearly vertical porous wall. *Journal of Engineering Mathematics*, 88(1), 49–66.
- Kao, J. H., Lee, J. F., & Yu-Chun, C. (2015). A direct coupling numerical method for solving three-dimensional interaction problems of wave and floating structures. *Engineering Analysis with Boundary Elements*, 55, 10–27.
- Koutandos, E., Prinos, P., & Gironella, X. (2005). Floating breakwaters under regular and irregular wave forcing: reflection and transmission characteristics. *Journal of Hydraulic Research*, 43(2), 174–188.
- Li, B., Cheng, L., Deeks, A. J., & Teng, B. (2005a). A modified scaled boundary finite-element method for problems with parallel side-faces. Part I. Theoretical developments. *Applied Ocean Research*, 27(4–5), 216–223.
- Li, B., Cheng, L., Deeks, A. J., & Teng, B. (2005b). A modified scaled boundary finite-element method for problems with parallel side-faces. Part II. Application and evaluation. *Applied Ocean Research*, 27(4–5), 224–234.
- Li, M., Guan, H., Zhang, H., & Liu, J. (2013a). Three-dimensional investigation of wave–pile group interaction using the scaled boundary finite element method—Part II: Application results. *Ocean engineering*, 64, 185–195.
- Li, M., Guan, H., Zhang, H., & Liu, J. (2013b). Three-dimensional investigation of wave-pile group interaction using the scaled boundary finite element method. Part I: Theoretical developments. *Ocean Engineering*, 64, 174–184.
- Liu, J., & Lin, G. (2013). Scaled boundary FEM solution of short-crested wave interaction with a concentric structure with double-layer arc-shaped perforated cylinders. *Computers and Fluids*, 79, 82–104.
- Meng, X. N., & Zou, Z. J. (2012). Wave interaction with a uniform porous cylinder of arbitrary shape. *Ocean Engineering*, 44, 90–99.
- Meng, X. N., & Zou, Z. J. (2013). Radiation and diffraction of water waves by an infinite horizontal structure with a sidewall using SBFEM. *Ocean Engineering*, 60, 193–199.
- Mohasseb, S., Moradi, M., Sokhansefat, T., Kasaeian, A., & Mahian, O. (2017). A novel approach to solve inverse heat conduction problems: Coupling scaled boundary finite element method to a hybrid optimization algorithm. *Engineering Analysis with Boundary Elements*, 84, 206–212.
- Ryu, S., Kim, M. H., & Lynett, P. J. (2003). Fully nonlinear wave-current interactions and kinematics by a BEM-based numerical wave tank. *Computational mechanics*, 32(4–6), 336–346.
- Sannasiraj, S. A., Sundaravadevelu, R., & Sundar, V. (2001). Diffraction–radiation of multiple floating structures in directional waves. *Ocean Engineering*, 28(2), 201–234.
- Seibi, A., & Al-Alawi, S. M. (1997). Prediction of fracture toughness using artificial neural networks (ANNs). *Engineering Fracture Mechanics*, 56(3), 311–319.
- Shahrabi, M., & Bargi, K. (2019). Enhancement the Fatigue Life of Floating Breakwater Mooring System Using Tuned Liquid Column Damper. *Latin American Journal of Solids and Structures*, 16(7).
- Song, Hao, & Tao, L. (2010). An efficient scaled boundary FEM model for wave interaction with a nonuniform porous cylinder. *International Journal for Numerical Methods in Fluids*, 63(1), 96–118.
- Song, Hao, & Tao, L. (2011). Wave interaction with an infinite long horizontal elliptical cylinder. *Proceedings of the International Conference on Offshore Mechanics and Arctic Engineering - OMAE*, 1, 589–597.
- Tao, L., Song, H., & Chakrabarti, S. (2007). Scaled boundary FEM solution of short-crested wave diffraction by a vertical cylinder. *Computer Methods in Applied Mechanics and Engineering*, 197(1–4), 232–242.

Tao, L., Song, H., & Chakrabarti, S. (2009). Scaled boundary FEM model for interaction of short-crested waves with a concentric porous cylindrical structure. *Journal of Waterway, Port, Coastal and Ocean Engineering*, 135(5), 200–212.

Taylor, R. E., & Zietsman, J. (1981). A comparison of localized finite element formulations for two-dimensional wave diffraction and radiation problems. *International Journal for Numerical Methods in Engineering*, 17(9), 1355–1384.

Turnbull, M. S., Borthwick, A. G. L., & Taylor, R. E. (2003). Wave–structure interaction using coupled structured–unstructured finite element meshes. *Applied Ocean Research*, 25(2), 63–77.

Zheng, Y. H., Shen, Y. M., You, Y. G., Wu, B. J., & Jie, D. S. (2004a). On the radiation and diffraction of water waves by a rectangular structure with a sidewall. *Ocean Engineering*, 31(17–18), 2087–2104.

Zheng, Y. H., You, Y. G., & Shen, Y. M. (2004b). On the radiation and diffraction of water waves by a rectangular buoy. *Ocean Engineering*, 31(8–9), 1063–1082.

Zhong, H., Li, H., Ooi, E. T., & Song, C. (2018). Hydraulic fracture at the dam-foundation interface using the scaled boundary finite element method coupled with the cohesive crack model. *Engineering Analysis with Boundary Elements*, 88, 41–53.

Appendix A:

For the sake of completeness, the solution process of SBFEM equations is given in the following. By introducing new variable $\{\chi(\xi)\}$ and substituting this variable and equation (11) into equation (10) yields:

$$(A.1) \xi\{\chi(\xi)\}_{,\xi} = [Z]\{\chi(\xi)\}$$

Where

$$(A.2) [Z] = \begin{bmatrix} -[E_0]^{-1}[E_1]^T & [E_0]^{-1} \\ [E_2] - [E_1][E_0]^{-1}[E_1]^T & [E_1][E_0]^{-1} \end{bmatrix}$$

Doubling the number of unknowns is occurred in this transformation. Postulating the solution in the form of $\{\chi(\xi)\} = \{\hat{\chi}\}\xi^{-\lambda}$ and putting this equation into equation (A.1) results in an Eigen-value problem as:

$$(A.3) -[Z]\{\hat{\chi}\} = \lambda\{\hat{\chi}\}$$

Where $\{\hat{\chi}\}$ includes nodal potential nodal flow amplitude as bellow:

$$(A.4) \{\hat{\chi}(\xi)\} = \begin{Bmatrix} \hat{a} \\ \hat{q} \end{Bmatrix}$$

and $\{\hat{q}\} = (-\lambda)[E_0]\{\hat{a}\} + [E_1]^T\{\hat{a}\}$. λ is modal scaling coefficient in radial direction. The equation (A.3) is represented in the following matrix form:

$$(A.5) -[Z][\hat{\chi}] = [\hat{\chi}][\Lambda]$$

where eigenvectors and eigenvalues are formed columns of $[\hat{\chi}]$ and diagonal entries of $[\Lambda]$, respectively. Sorting in descending order, two groups of eigenvalues with opposite sign, extracted from the Eigen-problem, are shown with $[\lambda_i]$ and $-[\lambda_i]$, while $\text{Re}(\lambda_i) \geq 0$. There is one zero eigenvalue in each two groups. Constant potential that is appeared in zero eigenvalue, means there is no flow in fluid domain. Therefore, eigenvectors corresponding to zero eigenvalues are linear dependent. Therefore, to the solution of equation (A.1), Jordan decomposition is employed as:

$$(A.6) [\bar{\Lambda}] = \begin{bmatrix} [\bar{\Lambda}_0] & & \\ & \begin{bmatrix} 0 & 1 \\ 0 & 0 \end{bmatrix} & \\ & & -[\bar{\Lambda}_0] \end{bmatrix}$$

$[\bar{\Lambda}_0]$ is a diagonal matrix similar to $[\lambda_i]$ which zero eigenvalue is removed. Considering transform matrix as $[T]$, the Eigen-problem is expressed as:

$$(A.7) -[Z][T] = [T][\bar{\Lambda}]$$

So the general form of solution can be written as:

$$(A.8) \{\chi(\xi)\} = [T]\xi^{[\Lambda]}\{c\}$$

where the constant vector $\{c\}$ constitute the each mode contribution in the solution. To put it another way, the resulting solution is the superposition of all potential modes. Subdividing eigenvector and diagonal exponential eigenvalue matrixes to $n \times n$ blocks as follow, the nodal potential and flow can be determined:

$$(A.9) \quad \{\chi(\xi)\} = \begin{bmatrix} [T_{11}] & [T_{12}] \\ [T_{21}] & [T_{22}] \end{bmatrix} \begin{bmatrix} \xi^{[\lambda_{pos}]} \\ \xi^{[\lambda_{neg}]} \end{bmatrix} \begin{Bmatrix} c_1 \\ c_2 \end{Bmatrix}$$

$c_2 = 0$ is intended to provide a finite value at the scaling center, thus the solution take the form:

$$(A.10) \quad \{a(\xi)\} = [T_{11}] \xi^{[\Lambda]} \{c_1\}$$

$$(A.11) \quad \{q(\xi)\} = [T_{21}] \xi^{[\Lambda]} \{c_1\}$$

Combining two last equations the result is written as:

$$(A.12) \quad \{q(\xi)\} = [H^b] \{a(\xi)\}$$

Where $[H^b] = [T_{21}][T_{11}]^{-1}$.

Appendix B

For the unbounded sub-domains, similar to the previous section, using the variable $\{\chi(\xi)\}$ and equation (13), the equation (12) is transformed as:

$$(B.1) \quad \{X(\xi)\}_{,\xi} = [Z] \{X(\xi)\}$$

Where $[Z]$ is defined as:

$$(B.2) \quad [Z] = \begin{bmatrix} -[E_0]^{-1}[E_1]^T & [E_0]^{-1} \\ [E_2] - [E_1][E_0]^{-1}[E_1]^T - \bar{k}^2[M_0] & [E_1][E_0]^{-1} \end{bmatrix}$$

Assuming the solution general form of equation (B.1) based on Li et al (2005a), as:

$$(B.3) \quad \{X(\xi)\} = [\Phi] e^{[\Lambda]\xi} \{c^\infty\}$$

By removing evanescent modes at far field boundary condition, the analytical solution of nodal potential and nodal flow in radial direction is obtained as:

$$(B.4) \quad \{a(\xi)\} = [\Phi_{12}] e^{[\lambda_j^-]\xi} \{c_2^\infty\}$$

$$(B.5) \quad \{q(\xi)\} = [\Phi_{22}] e^{[\lambda_j^-]\xi} \{c_2^\infty\}$$

Eliminating constant vector $\{c_2^\infty\}$ from equations (B.4) and (B.5) leads to:

$$(B.6) \quad [H^\infty] \{a(\xi)\} = \{q(\xi)\}$$

where $[H^\infty] = ([\Phi_{12}] e^{[\lambda_j^-]\xi})^{-1} ([\Phi_{22}] e^{[\lambda_j^-]\xi})$.